JOURNAL OF PROPULSION AND POWER
Vol. 31, No. 1, January–February 2015

D-149

Propellant Injector Influence on Liquid-Propellant Rocket Engine Instability

Pavel P. Popov,* William A. Sirignano,† and Athanasios Sideris‡
University of California, Irvine, Irvine, California 92697

DOI: 10.2514/1.B35400

The avoidance of acoustic instabilities, which may cause catastrophic failure, is demanded for liquid-propellant rocket engines. This occurs when the energy released by combustion amplifies acoustic disturbances; it is therefore essential to avoid such positive feedback. Although the energy addition mechanism operates in the combustion chamber, the propellant injector system may also have considerable influence on the stability characteristics of the overall system, with pressure disturbances in the combustion chamber propagating back and forth in the propellant injector channels. The introduced time delay may affect stability, depending on the ratio of the wave propagation time through the injector to the period of the combustion chambers acoustic modes. This study focuses on transverse-wave liquid-propellant rocket engine instabilities using a two-dimensional polar coordinate solver (with averaging in the axial direction) coupled to one-dimensional solutions in each of the coaxial oxygen–methane injectors. A blockage in one (or more) of the injectors is analyzed as a stochastic event that may cause an instability. A properly designed temporary blockage of one or more injectors can also be used for control of an oscillation introduced by any physical event. The stochastic and design variables parameter space is explored with the polynomial chaos expansion method.

Nomenclature

A_{chem}	=	chemical rate constant, $\text{m}^3/(\text{s}\cdot\text{kg})$
A_{entrance}	=	cross-sectional area of nozzle entrance, m^2
A_{throat}	=	cross-sectional area of nozzle throat, m^2
A, B	=	constants, defined in Eq. (2)
a	=	speed of sound, m/s
a, b	=	chemical rate constants
c_p	=	specific heat at constant pressure, $\text{J/K}\cdot\text{kg}$
c_v	=	specific heat at constant volume, $\text{J/K}\cdot\text{kg}$
D	=	mass diffusivity, m^2/s
E	=	energy release rate, $\text{J/kg}\cdot\text{s}$
j	=	index for Cartesian coordinates
L	=	chamber length, m
$\mathcal{L}(\cdot)$	=	general differential operator
p	=	pressure, newton m^{-2}
$Q_l^{(d)}$	=	Smolyak quadrature of lth order in d dimensions
R	=	chamber radius, m
R_s	=	mixture specific gas constant, $\text{J/kg}\cdot\text{K}$
R_i	=	inner radius of coaxial jet, m
R_o	=	outer radius of coaxial jet, m
R_u	=	universal gas constant, $\text{J/kg}\cdot\text{mole/K}$
r	=	radial position, m
s	=	specific entropy, $\text{J/K}\cdot\text{kg}$
T	=	temperature, K
t	=	time, s
U	=	coaxial jet velocity, m/s
u_r	=	radial velocity component, m/s
u_θ	=	tangential velocity component, m/s
Y_i	=	mass fraction of species i
α, β	=	Schvab–Zel'dovich variables
γ	=	ratio of specific heats
ϵ	=	activation energy, $\text{J/kg}\cdot\text{mole}$
η	=	local radial coordinate for the injector grids
θ	=	azimuthal position
ν	=	kinematic viscosity, m^2/s
ν_T	=	turbulent kinematic viscosity, m^2/s
$\boldsymbol{\xi}$	=	sample space coordinate of random variables
ρ	=	density, $\text{kg}\cdot\text{m}^{-3}$
τ_F	=	first tangential mode period, s
$\boldsymbol{\Psi}(\cdot)$	=	Legendre polynomials
ω_i	=	reaction rate of species i, s^{-1}
0	=	undisturbed state
$\langle\cdot\mid\cdot\rangle$	=	inner product

Subscripts

F	=	fuel
i	=	index for chemical species
j	=	index for Cartesian coordinates
m	=	properties in the intake manifold
O	=	oxidizer
0	=	undisturbed state

I. Introduction

WE ADDRESS the problem of liquid-propellant rocket engine (LPRE) combustion instability, which is a well-known phenomenon in rocket operation. The high-energy release by combustion can, in certain conditions, reinforce acoustic oscillations, causing them to grow to destructive amplitudes. LPRE combustion instability provides a very interesting nonlinear dynamics problem, as shown by both theory and experiment [1–3].

The combustion chamber, like any partially confined volume filled with gas, has an infinite number of natural acoustic resonant modes. In some operational domains, linear theory can predict that any small disturbance in the noise range can grow to a finite-amplitude limit-cycle acoustic oscillation driven by the combustion process. In another type of operational domain, any disturbance, whether in the noise range or substantially larger, will decay in time; the only limit cycle is the steady-state equilibrium. A third type of operational domain is one where both an unstable and a stable limit-cycle oscillation exist. That is, noise and larger disturbances up to some threshold level will decay with time. However, above that threshold level, disturbances will develop in time toward the stable limit-cycle oscillation, which has an amplitude higher than the threshold level given by the unstable limit cycle. Our attention here will focus on this bistable operating domain of the engine where the triggering is possible and both an unstable limit-cycle and a greater-amplitude stable limit cycle exist. Neighboring operating domains with

Presented as Paper 2014-0134 at the 52nd AIAA Aerospace Sciences Meeting, National Harbor, MD, 13–17 January 2014; received 3 April 2014; revision received 21 July 2014; accepted for publication 23 July 2014; published online 3 November 2014.

*Postdoctoral Fellow; ppopov@uci.edu. Member AIAA.
†Professor. Fellow AIAA.
‡Professor.

different design parameters (e.g., mean pressure, mass flow, and mixture ratio) can be unconditionally stable (i.e., with no limit-cycle oscillation) or unconditionally unstable (i.e., with a stable limit-cycle oscillation). This is shown in Fig. 1, which shows calculation results based on analyses given by Sirignano and Popov [3] and Popov et al [4]. It provides a stability diagram for a range of the injector velocity and reactant mixture fraction parameter variables. The top left graph shows values of the stable and unstable first tangential mode limit cycles as a function of the injector velocity. The top right graph shows values of the stable and unstable first tangential mode limit cycles as a function of the inner injector radius, for a fixed outer injector radius (stoichiometric proportions are achieved for an inner injector radius of 0.898 cm). The bottom graph shows a plot of stability regime types as a function of both mixture fraction and injector velocity. For a reduced injector velocity and very rich or very lean reactant mixtures, the overall system is unconditionally stable; and for an increased injector velocity at a stoichiometric mixture fraction, the overall system is unconditionally unstable.

The design parameters remain constant with time; consequently, drift will not occur from one domain to another during engine operation.

There are two general types of acoustical combustion instability: "driven" instability and "self-excited" instability, as noted by Culick [5], who describes evidence in some solid-propellant rockets of the driven type where noise or vortex shedding causes kinematic waves (i.e., waves carried with the moving gas) of vorticity or entropy to travel to some point where an acoustical reflection occurs. The reflected wave causes more noise or vortex shedding after traveling back, and a cyclic character results. These driven types do not rely on acoustical chamber resonance and are much smaller in amplitude, since the energy level is limited by the driving energy. The frequency of oscillation for cases where vortex shedding is a factor depends on two velocities: the sound speed and the subsonic, kinematic speed of the vortex. Consequently, the frequency is lower than a purely acoustic resonant frequency. Oscillations of this type are found in the longitudinal mode. To the best of our knowledge, these have never been observed in LPRE operation or in any transverse-mode instability and, when occurring in solid rockets or ramjets, the amplitudes are much lower than the values of concern for LPRE. So, they will not be addressed in this research.

Interest in propellant combinations of hydrocarbon fuel and oxygen, stored as liquids, is returning in the LPRE field. The analysis and results here will address situations where the methane and oxygen propellants are injected coaxially as gasses. These propellants will have elevated temperatures at the injectors because they have been used before injection, either for partial combustion for gas generation to drive a turbo pump or as a coolant. In particular, the inlet temperature and the mean combustion-chamber pressure were carefully chosen to place the mixture in the supercritical (i.e., compressible fluid) domain. Therefore, realism is maintained here when the chamber flow is treated as gaseous.

The dynamic coupling of the injector system with the combustion chamber of a liquid-propellant rocket engine has been a topic of interest for many decades. Two types of instabilities are known to occur. The chugging instability mode has nearly uniform but time-varying pressure in the combustion chamber. The combustion chamber acts as an accumulator or capacitor, whereas the inflowing propellant mass flux oscillates because the oscillating chamber pressure causes a flux-controlling oscillatory pressure drop across the injector. This low-frequency instability was characterized by Summerfield [6]. The second type of coupling involves a high-frequency oscillation at a near-resonant chamber mode frequency. Here, the resonant frequency has been modestly adjusted because the acoustic system involves some portion of the internal volume of the injector as well as the combustion chamber and convergent nozzle volumes. Crocco and Cheng [7] discussed both types of instability for one-dimensional (longitudinal) oscillations. Interesting discussions of coupled injector-system acoustics by Nestlerode, Fenwick, and Sack and by Harrje and Reardon can be found in pages 106–126 of the well-known NASA SP-194 [1]. More recent overviews and analyses are provided by Hutt and Rocker [8] and DeBenedictus and Ordonneau [9]. Yang et al. [10] provided several interesting papers on the design and modeling of rocket injector systems. Our work will focus on the high-frequency coupling of the transverse chamber

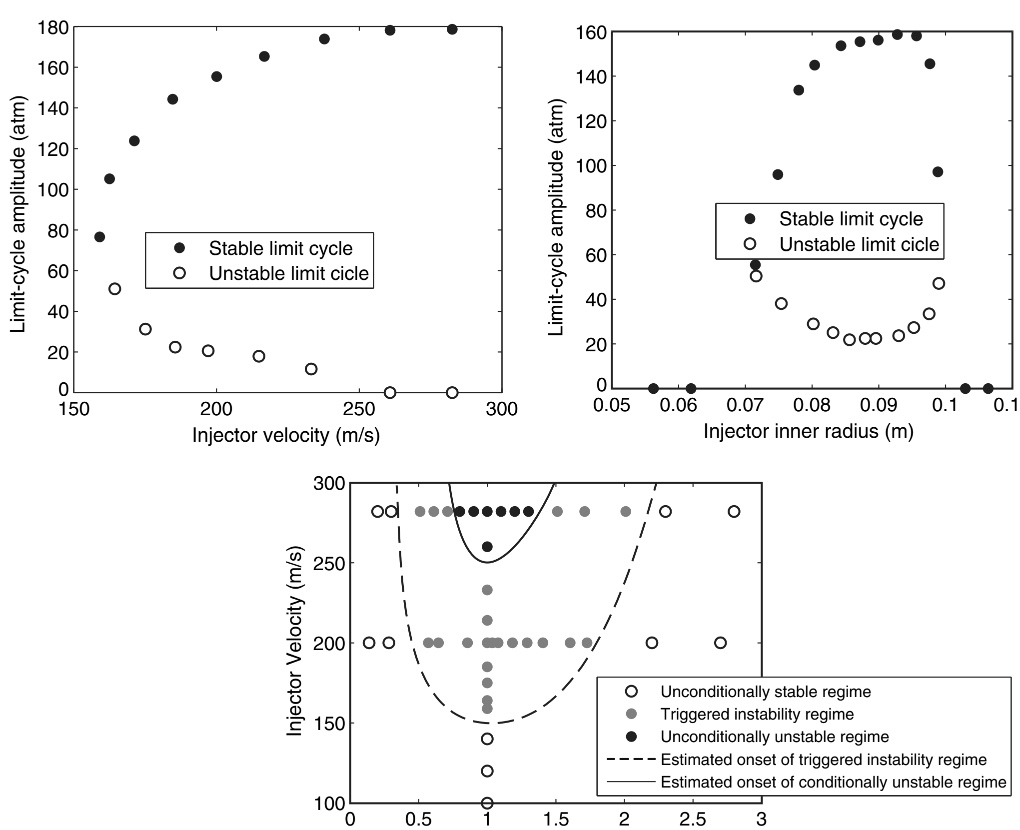

Fig. 1 System stability as a function of injector velocity and inner radius (mixture ratio).

oscillations with the injector but will differ from previous works in two ways. These previous works mostly used linear analysis, whereas we shall address the nonlinear dynamics. Furthermore, the analysis here will consider disruptions of the injector flow, both as potential triggers of nonlinear instability and as potential mechanisms for arresting a developing instability.

The disturbances that trigger combustion instability can result from fluid-mechanical disruptions in the propellant injection process, shedding in the combustion chamber of large rogue vortices that eventually flow through the choked nozzle [11], extraordinary excursions in local burning rates, or a synergism among such events. In the present work, we will consider the first of the aforementioned types of disturbances, namely, disturbances due to blockage in one or more of the injector ports. Such blockages are characterized by their magnitude, location, duration, and delay between each other. Typically, the rocket engineer does not know these characteristics a priori; therefore, these parameters bear uncertainty and may be described as stochastic variables. Thus, this nonlinear dynamics problem may properly be viewed as stochastic. In particular, the magnitude and duration of a blockage and, for the involvement of more than one port, the time delay between injector blockages are viewed as random variables.

To obtain an accurate solution to this stochastic problem in an efficient computational manner, we employ a polynomial chaos expansion (PCE) [12,13] that expresses the solution as a truncated series of polynomials in the random variables (RVs) characterizing injector blockage. The use of PCEs in terms of Hermite polynomials of Gaussian RVs was introduced by Wiener [14], and their convergence properties were studied by Cameron and Martin [15]. Nonlinear oscillations present a challenging application for PCE methods, as they have difficulty with approximating the long-term solution of dynamical equations; indeed, convergence of the PCE is not uniform with respect to the time variable. As it will be discussed later in detail, it is possible to capture the triggering of unstable oscillations with a modest number of terms in the PCE and do so at a computational cost considerably smaller than a more traditional Monte Carlo approach. Unlike the authors' previous work [4], which uses PCE exclusively for spanning the parameter space of random injector channel blockages, the present research also uses the PCE methodology to explore the parameter space of a single design variable, namely, the length of the injector channel, which has significant influence on the stability characteristics of the overall system.

In recent previous papers [3,4], a more detailed background and literature review was presented for combustion instability research and stochastic analysis. Consequently, a less detailed review is provided here.

In this paper, an analysis is presented of nonlinear transverse-mode combustion instability in a circular LPRE combustion chamber with acoustic coupling to a quasi-steady exit flow through many short, convergent, choked nozzles distributed over the exit cross section. In this way, it is similar to previous analyses [3,4]. Although the nozzle configuration deviates from practical designs, it has a long history of use in experiments and theory on account of its convenience [1,7]. A new aspect involves the nonlinear acoustic couplings with flows in the propellant injectors upstream of the chamber. In addition, triggering is examined through a stochastic analysis following our previous approach [4]. In practice, propellant flow through the injector can be in the same liquid phase as the stored propellant: in a gaseous form mixed with combustion products because of upstream flow through a preburner used for a propellant turbopump, or in gaseous form because the liquid propellant was used as a combustion-chamber-wall coolant upstream. We consider here gaseous coaxial flow of the pure propellants methane and oxygen, based on the last scenario.

The remainder of this paper is organized as follows: the governing equations for the wave dynamics and the jet mixing and reaction are introduced in Sec. II. The polynomial chaos expansion approximation to the stochastic solution is also described in Sec. II. Section III provides the details of the numerical solution and analytic expressions for the stochastic disturbances to the flow that possibly can trigger the large-amplitude transverse acoustic oscillation. Results are presented in Sec. IV.

II. Governing Equations

A. Deterministic Analysis

The present analysis focuses on pure tangential modes of oscillation without significant longitudinal effects. We neglect the viscous and diffusion terms in the development of the wave equation, as these processes act on much smaller length scales than those of the acoustic waves in the combustion chamber. The wave equation for pressure is averaged in the axial x direction to yield the following two-dimensional evolution equation for the longitudinal average of pressure [3]:

$$\begin{aligned}
&\frac{\partial^2 p}{\partial t^2} + A p^{(\gamma-1)/2\gamma}\frac{\partial p}{\partial t} - B p^{(\gamma-1)/\gamma}\left[\frac{\partial^2 p}{\partial r^2} + \frac{1}{r}\frac{\partial p}{\partial r} + \frac{1}{r^2}\frac{\partial^2 p}{\partial \theta^2}\right] \\
&= \frac{(\gamma-1)}{\gamma}\frac{1}{p}\left(\frac{\partial p}{\partial t}\right)^2 + (\gamma-1)\frac{\partial E}{\partial t} \\
&\quad + \gamma p^{(\gamma-1)/\gamma}\left[\frac{\partial^2 (p^{1/\gamma}u_r^2)}{\partial r^2} + \frac{2}{r}\frac{\partial (p^{1/\gamma}u_r^2)}{\partial r}\right. \\
&\quad + \frac{2}{r}\frac{\partial^2 (p^{1/\gamma}u_r u_\theta)}{\partial r \partial \theta} + \frac{2}{r^2}\frac{\partial (p^{1/\gamma}u_r u_\theta)}{\partial \theta} \\
&\quad \left. + \frac{1}{r^2}\frac{\partial^2 (p^{1/\gamma}u_\theta^2)}{\partial \theta^2} - \frac{1}{r}\frac{\partial (p^{1/\gamma}u_\theta^2)}{\partial r}\right] \qquad (1)
\end{aligned}$$

where r and θ are the radial and azimuthal coordinates, respectively; p denotes pressure; u denotes velocity; and γ is the specific heat ratio. E is the energy release rate, and A and B are constants dependent on the steady-state temperature and pressure, and the ratio between the throat and entrance areas of the nozzle:

$$\begin{aligned}
B &= \frac{a_0^2}{p_0^{(\gamma-1)/\gamma}} \\
A &= \frac{KB}{L} \\
K &= \frac{\gamma+1}{2\gamma}\frac{A_{\mathrm{throat}}}{A_{\mathrm{entrance}}}\left(\frac{\gamma}{R}\right)^{1/2}\left(\frac{\gamma+1}{2}\right)^{-((\gamma+1)/2(\gamma-1))}\frac{p_0^{(\gamma-1)/2\gamma}}{T_0^{1/2}} \qquad (2)
\end{aligned}$$

with p_0, T_0, and a_0 denoting, respectively, the pressure, temperature, and speed of sound of the undisturbed chamber; and A_{throat} and A_{entrance} are, respectively, the throat and entrance areas of the nozzle.

Neglecting viscous dissipation and turbulence–acoustic interactions, the two momentum equations are averaged in the axial direction to yield [3]

$$\begin{aligned}
\frac{\partial u_r}{\partial t} + u_r\frac{\partial u_r}{\partial r} + u_\theta\frac{1}{r}\frac{\partial u_r}{\partial \theta} - \frac{u_\theta^2}{r} + \frac{C}{p^{1/\gamma}}\frac{\partial p}{\partial r} &= 0 \\
\frac{\partial u_\theta}{\partial t} + u_r\frac{\partial u_\theta}{\partial r} + u_\theta\frac{1}{r}\frac{\partial u_\theta}{\partial \theta} + \frac{u_r u_\theta}{r} + \frac{C}{r p^{1/\gamma}}\frac{\partial p}{\partial \theta} &= 0 \qquad (3)
\end{aligned}$$

with $C = p_0^{1/\gamma}/\rho_0$.

It is desirable to use a physically reasonable but simple description of the wave dynamics for the gaseous flow in each of the several coaxial injectors. More elaborate studies of individual injectors are given in [16–20]. In the injector feed pipes, variations in the tangential direction are neglected; pressure and velocity evolve via the equations

$$\frac{\partial^2 p}{\partial t^2} - a^2\frac{\partial^2 p}{\partial x^2} = a^2\frac{\partial^2 (\rho u^2)}{\partial x^2} - \frac{\partial a^2}{\partial t}\frac{\partial (\rho u)}{\partial x} \qquad (4)$$

$$\frac{\partial u}{\partial t} + u\frac{\partial u}{\partial x} = -\frac{1}{\rho}\frac{\partial p}{\partial x} \qquad (5)$$

which are solved on 10 separate one-dimensional grids, one for each separate injector channel. To ensure a sufficient pressure drop from the intake manifold to the injector channels so that pressure fluctuations in the channels do not cause reverse flow, each injector pipe is modeled as being connected to the intake manifold via an orifice of area A_O smaller than the area A_I of the injector itself. Denoting the intake manifold pressure and sound speed as p_m and a_m, respectively; and with the convention that the injector channels each have length L_I and span the interval $[-L_I, 0]$ in the x direction, the velocity at the orifice exit, assuming isentropic flow, is equal to

$$u_{\text{orifice}} = c_D \times a_m \sqrt{\frac{2}{\gamma - 1}} \sqrt{1 - \left(\frac{p(-L_I, t)}{p_m}\right)^{(\gamma-1)/\gamma}} \tag{6}$$

where $C_D \in [0, 1]$ is a discharge coefficient accounting for flow friction and separation. By conservation of mass, the mean velocity at the intake manifold end of the injector channel is equal to

$$u(-L_I, t) = c_D \frac{A_O}{A_I} a_m \sqrt{\frac{2}{\gamma - 1}} \sqrt{1 - \left(\frac{p(-L_I, t)}{p_m}\right)^{(\gamma-1)/\gamma}} \tag{7}$$

To obtain the energy release rate E, we introduce the Shvab–Zel'dovich variable $\alpha = Y_F - \nu Y_O$, where Y_F and Y_O are the fuel and oxidizer mass fractions, respectively, with ν being the fuel-to-oxygen mass stoichiometric ratio. The variable

$$\beta = (Q/(c_p T_o))Y_F - T/T_o + (p/p_o)^{(\gamma-1)/\gamma}$$

is introduced. The variables α, β, and Y_F evolve by the following set of scalar transport equations:

$$\frac{\partial \alpha}{\partial t} + u_x \frac{\partial \alpha}{\partial x} + u_\eta \frac{\partial \alpha}{\partial \eta} - D\left[\frac{\partial^2 \alpha}{\partial \eta^2} + \frac{1}{\eta}\frac{\partial \alpha}{\partial \eta} + \frac{\partial^2 \alpha}{\partial x^2}\right] = 0 \tag{8}$$

$$\frac{\partial \beta}{\partial t} + u_x \frac{\partial \beta}{\partial x} + u_\eta \frac{\partial \beta}{\partial \eta} - D\left[\frac{\partial^2 \beta}{\partial \eta^2} + \frac{1}{\eta}\frac{\partial \beta}{\partial \eta} + \frac{\partial^2 \beta}{\partial x^2}\right] = 0 \tag{9}$$

and

$$\frac{\partial Y_F}{\partial t} + u_x \frac{\partial Y_F}{\partial x} + u_\eta \frac{\partial Y_F}{\partial \eta} - D\left[\frac{\partial^2 Y_F}{\partial \eta^2} + \frac{1}{\eta}\frac{\partial Y_F}{\partial \eta} + \frac{\partial^2 Y_F}{\partial x^2}\right] = \omega_F \tag{10}$$

In the preceding equation, x and η are, respectively, the axial and radial coordinates of one of several axisymmetric cylindrical grids coaxial with each injector, and the source term on the right-hand side of Eq. (10), following a one-step irreversible Arrhenius chemical mechanism, has the form

$$\begin{aligned}\omega_F &= A_{\text{chem}} \rho Y_O Y_F e^{-\epsilon/R_u T} \\ &= \frac{A_{\text{chem}} p_o}{\nu R_s T_o} \frac{p}{p_o} \frac{Y_F[Y_F - \alpha]}{(Q/c_p T_o)Y_F - \beta + (p/p_o)^{(\gamma-1)/\gamma}} \\ &\times \exp\left[\frac{\epsilon/R_u T_o}{(Q/c_p T_o)Y_F - \beta + (p/p_o)^{(\gamma-1)/\gamma}}\right]\end{aligned} \tag{11}$$

where A_{chem} is the chemical rate constant; ϵ is the activation energy; and R_s and R_u are, respectively, the mixture specific and universal gas constants. The present source term formulation has been compared with the classic Westbrook and Dryer one-step mechanism [21,22], which uses nonunitary exponents for the preexponential factors Y_O, Y_F, and no significant difference was observed for the present case.

The axial and radial velocities in Eqs. (8–10) are obtained from a solution of the variable-density Reynolds-averaged Navier–Stokes equations

$$\rho\left(\frac{\partial u_x}{\partial t} + u_x \frac{\partial u_x}{\partial x} + u_\eta \frac{\partial u_x}{\partial \eta}\right) = -\frac{\partial p_l}{\partial x} + \rho \nu_T \left[\frac{\partial^2 u_x}{\partial x^2} + \frac{1}{\eta}\frac{\partial}{\partial \eta}\left(\eta \frac{\partial u_x}{\partial \eta}\right)\right] \tag{12}$$

$$\begin{aligned}\rho\left(\frac{\partial u_\eta}{\partial t} + u_x \frac{\partial u_\eta}{\partial x} + u_\eta \frac{\partial u_\eta}{\partial \eta}\right) &= -\frac{\partial p_l}{\partial \eta} \\ &+ \rho \nu_T \left[\frac{\partial^2 u_\eta}{\partial x^2} + \frac{1}{\eta}\frac{\partial}{\partial \eta}\left(\eta \frac{\partial u_\eta}{\partial \eta}\right) - \frac{u_\eta}{\eta^2}\right]\end{aligned} \tag{13}$$

which are solved on each injector grid, where $p_l(x, \eta, t)$ is a local hydrodynamic pressure for which the mean is by definition 0 and which has considerably lower magnitude than the injector pressure $p(t)$ obtained from Eq. (1). The density in Eqs. (12) and (13) is obtained from the species scalars and the long-wavelength pressure $p(t)$ at the injector's location, so that the overall procedure for solving Eqs. (12) and (13) is elliptic.

The turbulent viscosity ν_T and diffusivity D are evaluated based on the turbulent viscosity approximation for a self-similar jet [23] with a turbulent Prandtl number of 0.7, yielding

$$\nu_T = \frac{U(t)R_o}{35} \tag{14}$$

$$D = \frac{U(t)R_o}{24.5} \tag{15}$$

where $U(t)$ is the magnitude of the vector formed by the jet exit velocity and the local transverse-wave-induced velocity.

B. Galerkin Approximation of a Stochastic Partial Differential Equation System with Uncertainty in the Initial Conditions

We use the polynomial chaos expansion method, previously applied by the authors in [4] to a similar problem dealing only with the combustion-chamber wave dynamics. Let the perturbation from steady-state operating conditions be uniquely determined by a vector, $\boldsymbol{\xi}$, of independent random variables or geometrical parameters, such as the length of the injector pipe.

Then, the solution of the system of partial differential equations (PDEs) from the previous subsection, consisting of the fields p, u_i, α, β, and Y_F may be expressed as a set of fields, in the forms $[p, u_i] = \boldsymbol{n}(r, \theta, t, \boldsymbol{\xi})$ and $[\alpha^{(j)}, \beta^{(j)}, Y_F^{(j)}] = \boldsymbol{m}(x, \eta, t, \boldsymbol{\xi})$, with the superscript (j) denoting each of the 10 injectors, and so the system of Eqs. (1) and (3) forms two multivariate PDE systems [4]:

$$\mathcal{L}_1(\boldsymbol{n}, r, \theta, t, \boldsymbol{\xi}) = \boldsymbol{f}_1(r, \theta, t, \boldsymbol{m}, \boldsymbol{\xi}) \tag{16}$$

$$\mathcal{L}_2(\boldsymbol{m}, x, \eta, t, \boldsymbol{\xi}) = \boldsymbol{f}_2(x, \eta, t, \boldsymbol{n}, \boldsymbol{\xi}) \tag{17}$$

where Eq. (16) governs the evolution of p, u_r, and u_θ on a two-dimensional $r - \theta$ grid. Equation (17) governs the evolution of 10 sets (one for each injector) of the fields α, β, and Y_F on two-dimensional $x - \eta$ grids, coaxial with the injector axes. $\mathcal{L}_1$ and $\mathcal{L}_2$ are the differential operators representing Eqs. (1) and (3) and Eqs. (8–10) respectively, and $\boldsymbol{f}_1$, $\boldsymbol{f}_2$ are source terms. Note that Eqs. (16) and (17) are coupled via the dependence on $\boldsymbol{m}$ of $\boldsymbol{f}_1$, the source term in the evolution equation of $\boldsymbol{n}$ (due to the pressure being dependent on the energy release) and, conversely, via the dependence on $\boldsymbol{n}$ of $\boldsymbol{f}_2$ (due to the Y_F source term being dependent on pressure). We shall employ the stochastic Galerkin methodology to approximate the solution of Eq. (16). For an in-depth introduction to the stochastic Galerkin technique, the reader is referred to [12,13].

A truncated polynomial chaos expansion consists of the approximations

$$\boldsymbol{n}(r,\theta,t,\boldsymbol{\xi}) \approx \sum_{k=0}^{P} \boldsymbol{n}_k(r,\theta,t)\Psi_k(\boldsymbol{\xi})$$
$$\boldsymbol{m}(x,\eta,t,\boldsymbol{\xi}) \approx \sum_{k=0}^{P} \boldsymbol{m}_k(x,\eta,t)\Psi_k(\boldsymbol{\xi}) \tag{18}$$

where $\Psi_k(\boldsymbol{\xi})$ are $P+1$ Legendre polynomials in the random vector $\boldsymbol{\xi}$. In particular, for the present case that uses uniform random variables, $\Psi_k(\boldsymbol{\xi})$ are all possible n-dimensional products, of a degree up to l for the lth-order PCE expansion, in the Legendre polynomials of the component scalars of $\boldsymbol{\xi}$. For a fixed simulation end time T_F and additional smoothness assumptions, this representation of the sample space implies exponential [13] convergence with respect to the order, l, of the PCE expansion. The number of polynomials, $P+1$, is equal to $(n+l)!/(n!l!)$. For the low-dimensional sample space used in this study, the PCE methodology has substantially better computational efficiency than a more standard Monte Carlo procedure [4].

Substituting the approximation of Eq. (18) into Eqs. (16) and (17), and taking the inner product denoted by $\langle \cdot \mid \cdot \rangle$ over the range of $\boldsymbol{\xi}$ with each of the polynomials $\Psi_k(\boldsymbol{\xi})$, yields

$$\left\langle \mathcal{L}_1\left(r,\theta,t,\boldsymbol{\xi};\sum_{k=0}^{P}\boldsymbol{n}_k(r,\theta,t)\Psi_k(\boldsymbol{\xi})\right)|\Psi_i(\boldsymbol{\xi})\right\rangle = \langle \boldsymbol{f}_1(r,\theta,t,\boldsymbol{m},\boldsymbol{\xi})|\Psi_i(\boldsymbol{\xi})\rangle \tag{19}$$

$$\left\langle \mathcal{L}_2\left(x,\eta,t,\boldsymbol{\xi};\sum_{k=0}^{P}\boldsymbol{m}_k(x,\eta,t)\Psi_k(\boldsymbol{\xi})\right)|\Psi_i(\boldsymbol{\xi})\right\rangle = \langle \boldsymbol{f}_2(x,\eta,t,\boldsymbol{n},\boldsymbol{\xi})|\Psi_i(\boldsymbol{\xi})\rangle \tag{20}$$

which are two systems of $P+1$ deterministic equations, each similar to the system of equations [Eqs. (1–10)], which can be solved numerically for each of the $P+1$ coefficients $\boldsymbol{n}_k(r,\theta,t)$ and $\boldsymbol{m}_k(x,\eta,t)$ using the same discretization schemes used for the approximation of a deterministic solution to Eqs. (1–10).

A sparse grid based on Smolyak's quadrature rule is used to deal with the integration of the nonlinear terms when evaluating the inner products of Eqs. (19) and (20). In particular, we use $Q_i^{(1)}f$ to denote the ith order of a univariate nested quadrature rule [24], i.e.,

$$Q_i^{(1)}f = \sum_j q_{i,j} f(x_{i,j}) \tag{21}$$

where $q_{i,j}$ and $x_{i,j}$ are, respectively, the weights and nodes of the ith-order univariate quadrature, with $Q_0^{(1)}f$ being identically zero.

We use $Q^{(d_1)} \times Q^{(d_2)}g$ to denote the product of the multivariate quadratures $Q^{(d_1)}$ and $Q^{(d_2)}$: the first of which integrates on the first d_1 arguments, and the second Q^{d_2} of which integrates on the last d_2 arguments of a multivariate function g. Then, the d-dimensional, lth order of the sparse Smolyak quadrature, denoted $Q_l^{(d)}f$, is defined recursively as

$$Q_l^{(d)}f = \sum_{i=1}^{l}(Q_i^{(1)} - Q_{i-1}^{(1)}) \times Q_{l-i+1}^{(d-1)}f \tag{22}$$

With this multidimensional quadrature, we can approximate the inner product of, for example, the source term ω_F by expressing it as a function of $\boldsymbol{m}(\boldsymbol{\xi})$ and $\boldsymbol{n}(\boldsymbol{\xi})$, which are obtained from the polynomial expansion [Eq. (18)]. This gives us $\omega_F(\boldsymbol{\xi})$, and the inner product $\langle\omega_F(\boldsymbol{\xi})|\Psi_k(\boldsymbol{\xi})\rangle$ is approximated by

$$\langle\omega_F(\boldsymbol{\xi})|\Psi_k(\boldsymbol{\xi})\rangle \approx Q_l^{(d)}(\omega_F(\boldsymbol{\xi})\Psi_k(\boldsymbol{\xi})) \tag{23}$$

where the lth-order quadrature $Q_l^{(d)}$ is used to integrate on the d-dimensional sample space variable $\boldsymbol{\xi}$.

The use of the Smolyak quadrature yields, for smooth functions f, exponential convergence of the numerical error with respect to the order l of the quadrature $Q_l^{(d)}f$. Further, since it is based on only those points of the d-dimensional product of the univariate quadratures $Q_l^{(1)}$ which yield product quadratures of order l or less (whereas a standard d-dimensional product of the univariate quadratures yields product quadratures of order ld), the Smolyak quadrature $Q_l^{(d)}f$ involves evaluation on considerably fewer points than a simple product of univariate quadratures. To match the accuracy of the Smolyak quadrature to that of the PCE, we use the same order for both; for the seventh-order four-dimensional case considered next, a simple product of the seventh-order 15-point nested univariate quadratures would require $15^4 = 50{,}625$ points, whereas the Smolyak quadrature yielded by Eq. (22) requires only 641 points.

III. Simulation

Combustion instability was studied over a range of operating conditions for a 10-injector design by [3]. With varying mixture ratio or mass flow, three zones of stability type were found: stable operation under any perturbation; linearly (spontaneously) unstable with infinitesimal perturbation (noise) resulting in nonlinear limit-cycle oscillation; and an operating zone where triggering occurs with a disturbance above a threshold magnitude, leading to a nonlinear limit-cycle oscillation, while a perturbation below the threshold decays. Here, our stochastic analysis will focus on this last operating regime where triggering action is possible.

The present simulation uses a cylindrical chamber of axial length $L = 0.5$ m and radius $R = 0.14$ m, with 10 injectors: one at the center of the chamber; three at $r = R/2$, spaced apart at even angles of $2\pi/3$; and six at $r = 3R/4$, evenly spaced apart at angles of $\pi/3$. Each injector consists of two concentric pipes, as shown in Fig. 2: the inner of which, with a radius of 0.898 cm, serves as the oxidizer inlet; and the outer, with a radius of 1.1 cm, serves as the fuel inlet, leading to fuel and oxidizer inflow in stoichiometric proportions. The injector configuration is shown on the left-hand side of Fig. 3.

The fuel and oxidizer in the present simulation are, respectively, gaseous-phase methane and oxygen, entering the combustion chamber at 400 K with an axial velocity (at standard operating conditions) of 200 m/s. Using a value of 0.115 for the ratio between the nozzle throat area and the combustion-chamber cross-sectional area results in a steady-state operational pressure of 200 atm and a steady-state temperature of 2000 K.

The evolution equations for pressure and velocity [Eqs. (1) and (3)] are solved via a second-order finite difference procedure on a uniform polar grid, with the radial and azimuthal components of velocity staggered with respect to pressure. The evolution equations for the scalars α, β, and Y_F are solved on 10 disjoint two-dimensional

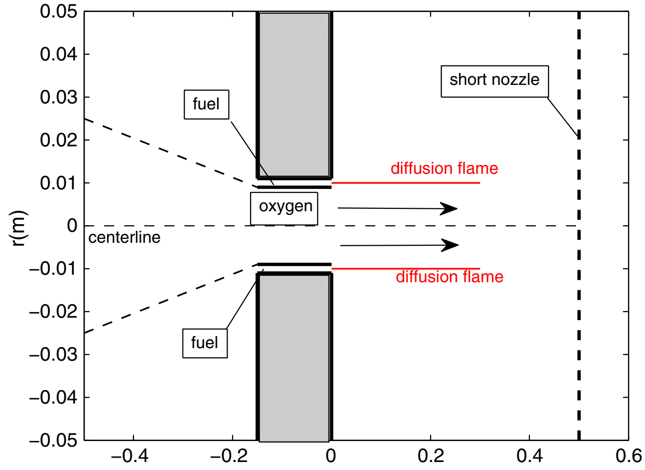

Fig. 2 Injector geometry: intake manifold ($x < -0.15$ m), injector channels (-0.15 m $\leq x \leq 0$), and chamber ($x > 0$).

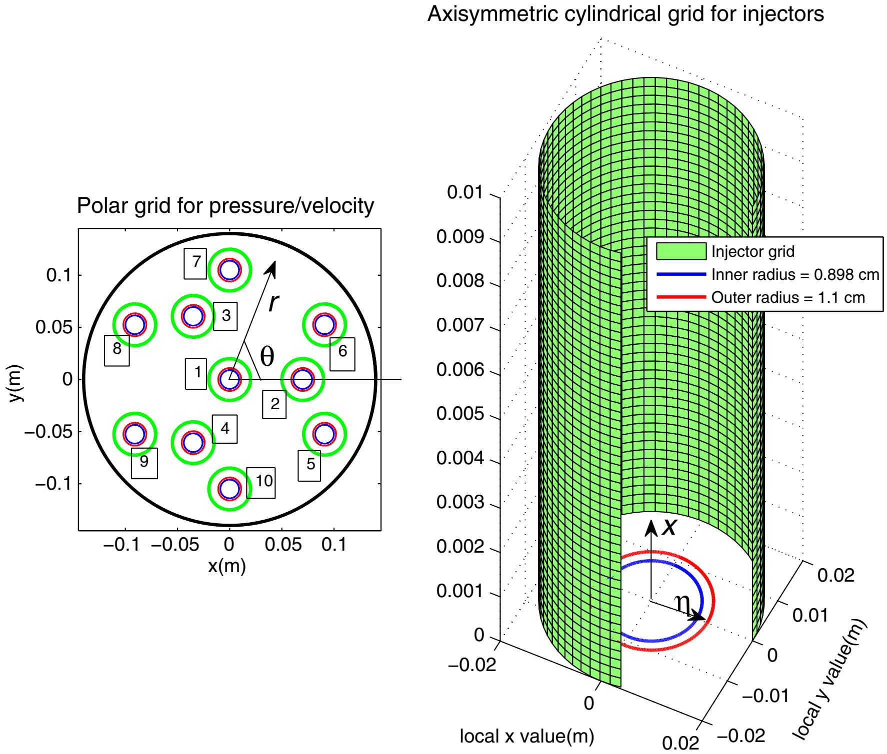

Fig. 3 Polar grid for chamber pressure and velocity. Axisymmetric grids for injector flows.

cylindrical grids (neglecting field variations in the azimuthal variable): each coaxial with the axis of the respective injector. For more details on the solution procedure for the deterministic system, the reader is referred to [3].

The evolution equations for pressure and velocity in the injector channels [Eqs. (4–7)] are solved on 10 separate one-dimensional grids for each injector channel (see Fig. 3). These solutions depend on the tangential pressure and velocity solutions of Eqs. (1) and (3) for determination of the pressure value at the end of the injector channel and provide the injector outlet velocities for the evolution equations for the scalars α, β, and Y_F.

In this study, we explore perturbations from standard operating conditions due to blockages in the flow from the intake manifold to the injector channels. Upstream of the injector channels, there exist turbopumps and flow turns. These features can produce cavitation or shed vortices. Those disturbances can advect downstream and cause blockages entering the injector, which are modeled simply by abrupt changes in the discharge coefficient of Eq. (7) applied at the upstream end of the injector channel. Specifically, we use an area ratio of $A_O/A_I = 0.5$ between the intake manifold orifice and the injector channel's cross section. An unobstructed flow is modeled by $C_D = 1$ for the discharge coefficient, and blockages are modeled as temporary decreases of the discharge coefficient to a certain minimal value. Specifically, a blockage of duration τ_B and peak mass flow reduction of $k \in [0, 1]$ correspond to a decrease in the discharge coefficient as a function of time according to the formula

$$c_D = 1 - k \sin(\pi t/\tau_B)^2 \tag{24}$$

We note that such a temporary reduction of the discharge coefficient causes a decrease and subsequent increase in the propellant flow rate for the corresponding injector, leading to a full sinusoidal cycle in the rate of change of energy release, $\frac{\partial E}{\partial t}$, which appears as a source term in Eq. (1). Thus, a blockage of period τ is expected to excite the combustion chamber's acoustic modes of similar period. To test the possibility for excitation of higher tangential mode instabilities, deterministic simulations with a square pulse in the discharge coefficient were also performed. Such a pulse contains higher-frequency components, which specifically excite a second tangential mode of considerable amplitude in the transient to the limit cycle. This component, however, decays by the time the limit cycle is achieved so that, for pulses with higher-frequency components, the limit cycle (if one is achieved and the oscillation does not decay to the standard operating conditions) is still dominated by the first tangential acoustic mode of this chamber for the chosen design parameters.

In addition to injector blockages as a source for triggered instability, we explore their use as a mechanism for the reduction of a growing instability. Specifically, we apply a controlled blockage after a moderate interval of time (accounting for the delay inherent in detection of an instability and response to it) has elapsed since the triggering event.

IV. Results

In this section, we explore the types of blockages that lead to the development of instabilities and their subsequent suppression. First, we present PCE simulations exploring a parameter space of possible injector disturbances that lead to instability. Then, we present results from simulations in which subsequent blockages, intentionally generated as part of a control mechanism, yield a return of the growing instability to the standard operating conditions.

A. Conditions Leading to the Development of a Limit Cycle

Here, we explore instabilities caused by a blockage in two adjacent injector channels, namely, injectors 9 and 10, as identified in Fig. 3, in the outer injector ring. We use the PCE methodology to obtain solutions for a four-dimensional random variable $\boldsymbol{\xi} = [\xi_1, \xi_2, \xi_3, \xi_4]$. The components $\xi_1, \ldots, \xi_4$ are independent and uniformly distributed on the interval [0,1]; they determine the blockage duration and magnitude as defined in Eq. (24), the delay between the blockages of injectors 9 and 10, as well as the design parameter of the injector length. Specifically, we have that $\xi_1 = k$ and $\tau_B = (0.5 + \xi_2)\tau_F$, where k and τ_B are, respectively, the blockage magnitudes and duration, as defined in Eq. (24); the delay between the two blockages is equal to $\xi_3 \times 2.5\tau_F$, and the injector length is equal to $0.11\ \mathrm{m} + 0.055\ \mathrm{m} \times \xi_4$.

Figure 4 plots the marginal probability of growth as a function of the duration of the injector blockage. It can be seen that this probability is highest when τ_B is close to τ_F, the period of the first tangential mode, with a probability of 0.67 at $\tau_B = \tau_F$. This is to be expected, since an injector blockage influences the pressure evolution equation via the $\frac{dE}{dt}$ source term in Eq. (1): this term is negative during the first half of the blockage, which causes a reduction of the oxygen mass flow rate, and hence a reduction of the heat release. During the second part of the blockage, the mass flow rate and heat release return to their original values, yielding a positive $\frac{dE}{dt}$. Therefore, a blockage of duration τ_B causes a perturbation of sinusoidal nature and the same period, in the source term $\frac{dE}{dt}$. This situation is most likely to excite an instability when τ_B matches the period of the most unstable mode for this chamber, namely, the first tangential mode.

Figure 5 presents marginal probability as a function of the maximal decrease of the oxygen flow rate. As can be expected, the probability increases for a stronger blockage, with a probability of 0.68 observed for a blockage during which the mass flow rate in the injector drops to zero. Note that, even for infinitesimal blockages (that is, maximal decrease close to 0), the probability of growth is positive: approximately 0.05. This, combined with the results of Fig. 6, implies that, for certain injector channel lengths, the overall system of the combustion chamber and injector is linearly unstable.

Probabilities of growth vs injector channel length are shown in Fig. 6. The length ranges from 0.11 m, for which the period of the pipe's first longitudinal mode matches τ_F, to 0.165 m, for which the first longitudinal mode's period is equal to $3/2\tau_F$. As can be expected, the system is less stable in the former case, which features a resonance between the injector feed and chamber acoustics. As previously mentioned, the probability of growth equals one for a pipe length of 0.11 m, suggesting that the system may be linearly unstable for that configuration. This result is supported by deterministic simulations performed for this injector length, which result in the development of an instability regardless of the magnitude of the injector blockage.

In addition to the probability of growth to the limit cycle, the length of the injector also influences the limit-cycle magnitude. This can be seen in Fig. 7, which plots limit-cycle magnitude vs injector length. There is a monotonic decrease of the limit-cycle amplitude, from 167 atm for the most unstable configuration with an injector length of 0.11 mm to 142 atm for an injector of length 0.165 m.

We also examine the influence of the time delay between the two blockages on the probability of growth. Figure 8 shows, for set injector lengths of 0.13 and 0.15 m, the probability of growth as a function of the time delay between the first and second blockages. It can be seen that the probability is decreased for time delays that are an odd multiple of $\tau_F/2$, and this decrease diminishes with increasing time delay. This is consistent with the deterministic results of the previous sections, in which a single antipulse was not sufficient to

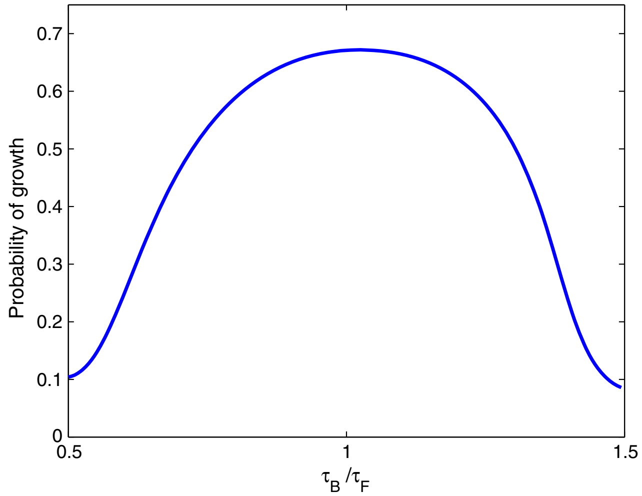

Fig. 4 Probability of growth to a limit cycle as a function of the blockage period τ_B.

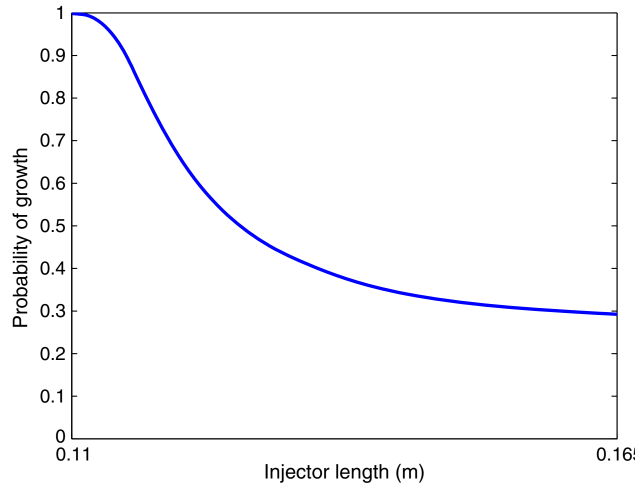

Fig. 6 Probability of growth as a function of the injector length.

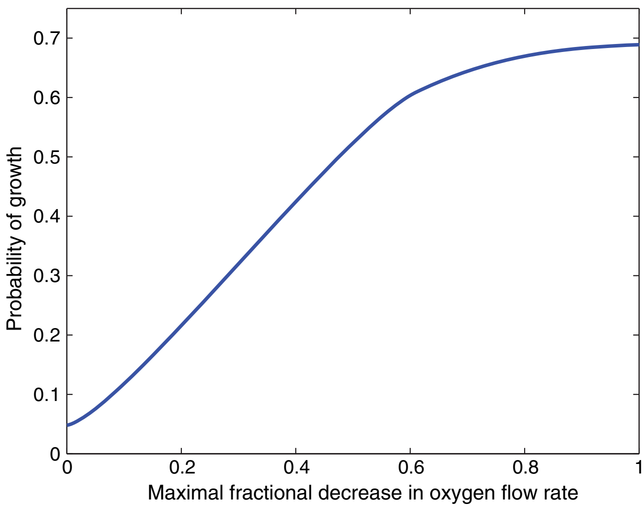

Fig. 5 Probability of growth to a limit cycle as a function of the fractional reduction of the oxygen flow rate.

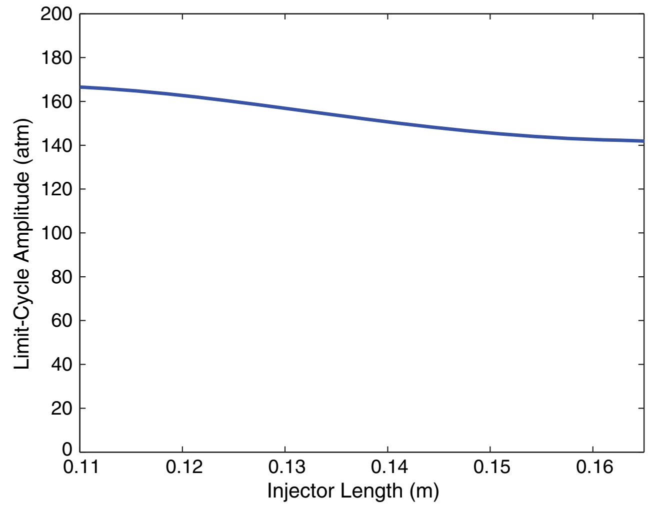

Fig. 7 Peak-to-peak amplitude of the limit cycle as a function of the injector length.

arrest the instability once it had grown considerably. We note that, in Fig. 8, although the overall probability of growth is larger for the more unstable, shorter injector length, this case also yields a larger decrease in the growth probability for delay times of $3\tau_F/2$ and $5\tau_F/2$.

The time delay between the two blockages also determines the type of first tangential limit cycle, when one develops. In particular, when the time delay is close to 0 (modulo τ_F), the limit cycle has the shape of a standing wave; whereas for time delays closer (modulo τ_F) to $\tau_F/6$ and $5\tau_F/6$, the limit cycle has the form of a spinning wave, traveling in the counterclockwise direction and clockwise direction, respectively.

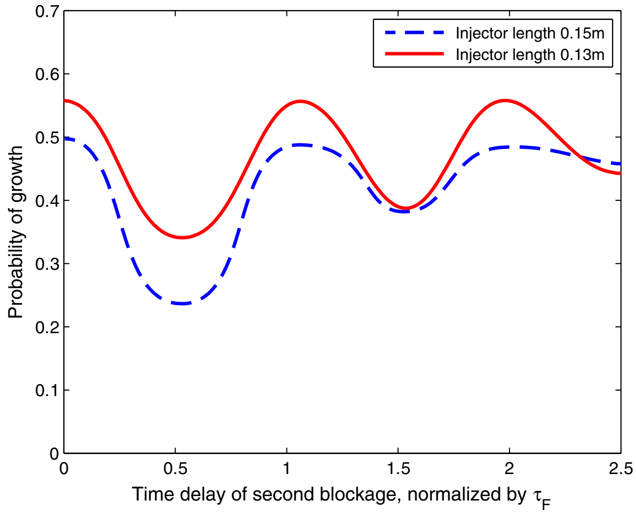

Fig. 8 Probability of growth as a function of the time delay between the two blockages.

Figure 9 shows, for the injector length of 0.135 m, a pressure contour plot of the fully developed limit cycle in the polar, axially averaged acoustic solver grid, as well as a contour plot of temperature in one of the cylindrical injector grids at standard operating conditions. The somewhat irregular shape of the pressure contour plot is due to the fact that the limit cycle contains acoustic modes of lower amplitude, in addition to the first tangential: specifically, a second tangential mode and a subharmonic; the reader is referred to [3] for a detailed spectral description of the acoustic limit cycle for this configuration. On the temperature contour plot, a diffusion flame is seen to develop in the mixing layer between oxidizer, fuel, and hot coflow streams.

Figure 10 shows a snapshot of the pressure and velocity distributions in one of the injectors at $r = 3/4R$: a longitudinal acoustic wave of length four times the injector length can be observed. This result is consistent with a classical quarter-wave tube with one open end and one closed end.

To explore interactions between other injector pairs, we perform a set of lower-dimensional PCE simulations, in which the blockage duration is set to equal τ_F, and the rest of the sample space variables vary in the same fashion as the simulation presented previously. Table 1 presents the sensitivity of each possible injector pair, in terms of the overall possibility of growth. As can be seen on this table, the most sensitive cases are those that feature at least one injector on the outer ring. We also note that the central injector has little effect on the

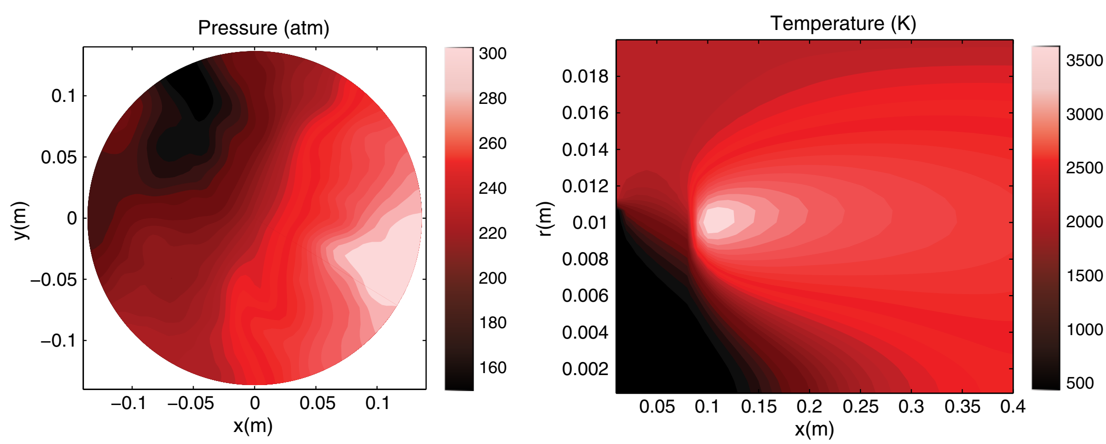

Fig. 9 Limit-cycle chamber pressure (left). Temperature on cylindrical grid at standard operation (right).

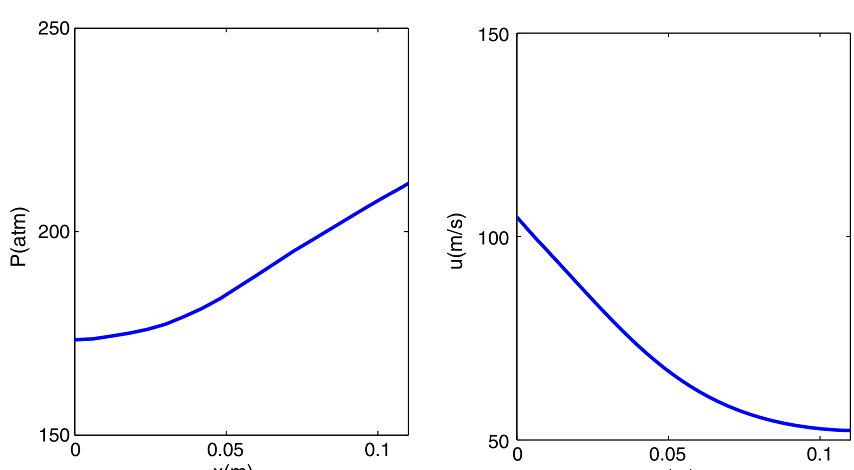

Fig. 10 Axial plot of instantaneous pressure in outer injector at limit cycle (left). Axial plot of axial velocity in the injector at the same time (right).

Table 1 Summary of probabilities and types of instability encountered for all possible injector pairs (not including mirrored configurations)

Injector pair	Probability of growth	Standing wave	Spinning wave
1-1 (both inner ring)	0	No	No
1-2 (inner/middle ring)	0.271	Yes	No
2-2 (same injector in middle ring)	0.245	Yes	No
2-3 (separate injectors in middle ring)	0.326	Yes	Yes
1-5 (inner and outer ring)	0.482	Yes	No
2-6 (middle and outer ring)	0.619	Yes	Yes
2-7 (middle and outer ring)	0.563	Yes	Yes
2-8 (middle and outer ring)	0.507	Yes	No
9-9 (same injector outer ring)	0.498	Yes	No
9-10 (separate injectors in outer ring)	0.671	Yes	Yes
9-5 (separate injectors in outer ring)	0.622	Yes	Yes
9-6 (opposite injectors in outer ring)	0.573	Yes	No

stability of the system, with no possibility of growth to a limit cycle when both blockages occur in this injector.

B. Potential for Active Control and Suppression of the Developing Limit Cycle

In the previous subsection, we observed that blockages in one or more of the offcenter injectors may lead to the development of an instability. Here, we consider the potential for active control via intentionally generated blockages, in order to reduce a growing instability back to the initial operating conditions. We do not necessarily advocate that injector blockage would be an optimal or even acceptable method of control. Rather, the point is to show that a designed disruption can be effective in countering a developing instability. First, we shall consider a set of deterministic simulations in which two or more "pulses" are introduced into the chamber.

Specifically, we shall denote a single pulse to be a blockage in injector 9 (as labeled in Fig. 3), of duration τ_F and peak mass flow reduction of 90%, followed by a blockage in injector 10, of the same duration and mass flow reduction. The time delay between these two blockages is $\tau_F/6$, which, combined with the durations for τ_F chosen here, causes the development of a traveling first tangential limit cycle.

We are interested in using a similar pair of blockages (or more than one pair) in order to suppress the growing instability and return the system to standard operating conditions. To this end, simulations have been performed in which an additional pair of blockages in injectors 9 and 10 have been introduced to the system, with a time delay from the first pair ranging between τ_F and $10\tau_F$ (note that the minimal time delay of τ_F is dictated by the chosen blockage durations). We consider these subsequent blockages to be "antipulses," which can be viewed as a potential control mechanism for bringing the system back into its normal operating condition.

It has been found that the subsequent pair of blockages can bring the system back to the original operating conditions, but only if it occurs soon after the first pulse and is approximately $\tau_F/2$ out of phase with it. As can be seen in Fig. 11, a single antipulse with a delay of $3\tau_F/2$ can arrest the growth of the developing instability. However, antipulses of longer time delay from the initial perturbation (even when they are $\tau_F/2$ out of phase with it) can only reduce the magnitude of the developing instability, after which it starts growing again.

In Fig. 11, we see that, even though single antipulses with a delay of $5\tau_F/2$ and larger are unsuccessful in causing a decay to 200 atm, they do reduce the energy of the growing instability. This suggests that a combination of more than one antipulse can stabilize the system even after a long time delay. To explore this possibility, we have chosen the case with an antipulse for which the time delay is $17\tau_F/2$,

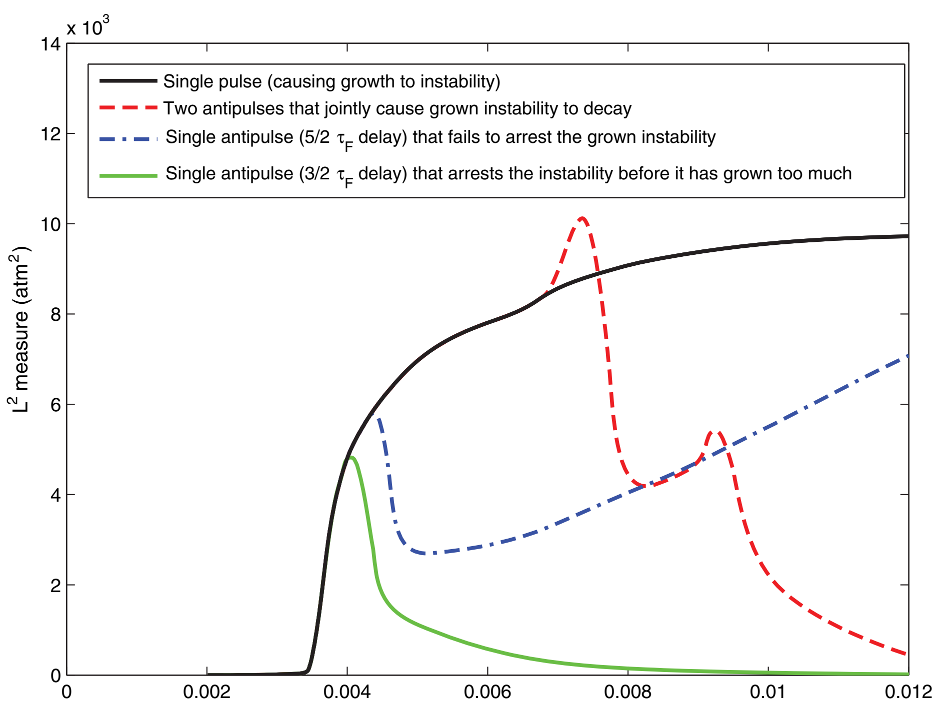

Fig. 11 L^2 **norm of pressure deviation from the standard operating condition of 200 atm, for a set of deterministic simulations with one or more injector blockages in the outer ring.**

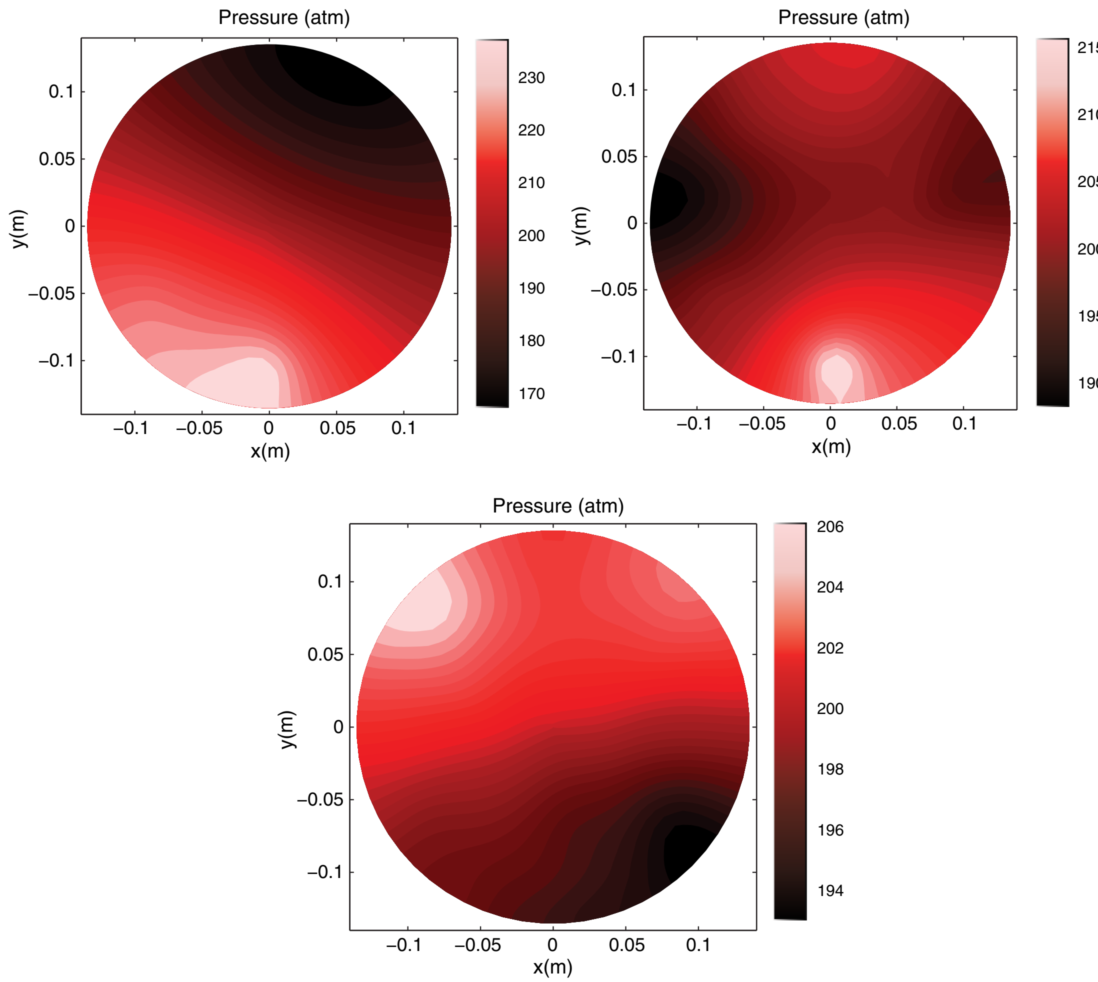

Fig. 12 Pressure for decay toward normal conditions caused by antipulse of time delay $3\tau_F/2$.

and we have run a set of simulations adding an additional antipulse, with a delay of $19\tau_F/2$ to $29\tau_F/2$.

The addition of the second antipulse can bring about a decay to equilibrium, provided that it follows quickly after the first. In particular, additional antipulses for which the delay is either close to $19\tau_F/2$ or $21\tau_F/2$ (the latter of which is shown in Fig. 11), can reinforce the first antipulse sufficiently to cause a decay to 200 atm.

From these results, it can be concluded that a blockage in the injector can act not only as a destabilizing mechanism but also as a control mechanism aimed at returning the combustion chamber back to its normal operating conditions once an instability has been detected. Based on the results of the simulations presented here, there are two possible avenues toward achieving this goal: either a single blockage-induced antipulse that is introduced sufficiently quickly after the destabilizing event or a set of antipulses, close in time to each other, to jointly reduce the energy of a higher-amplitude instability, after a longer time delay.

Figure 12 provides contour plots of the simulation with a $3\tau_F/2$ antipulse. In it, we can see the original spinning wave caused by the first pair of blockages and its disruption by the antipulse. The top left plot shows the initial traveling wave caused by the first pair of blockages. The top right plot shows the second blockage pair disrupting the traveling wave. The bottom plot shows the decaying wave after antipulse caused by the second blockage pair. The resulting pressure wave, in the shape of a first tangential spinning wave, has a magnitude below the triggering value and thus decays to zero amplitude at the mean value of 200 atm.

To encompass a larger parameter space, we also present results for a PCE simulation that, similar to the aforementioned deterministic results, deals with two pairs of blockages, each of which takes place in injectors 9 and 10 with a time delay of $\tau_F/6$ between them. The sample space variables are the magnitude of the first pair of blockages, which varies uniformly between 0 and 1; the magnitude of the second pair, similarly varying between 0 and 1; and the time delay between the two pairs ranging from 0 to $5\tau_F/2$. First, we shall consider the conditional probability that the second pulse will return the system to equilibrium, conditional upon the first pulse being strong enough to set up a limit cycle. Figure 13 plots the conditional probability of decrease to equilibrium as a function of the magnitude of the second pulse pair: as can be expected, this probability increases for a stronger antipulse.

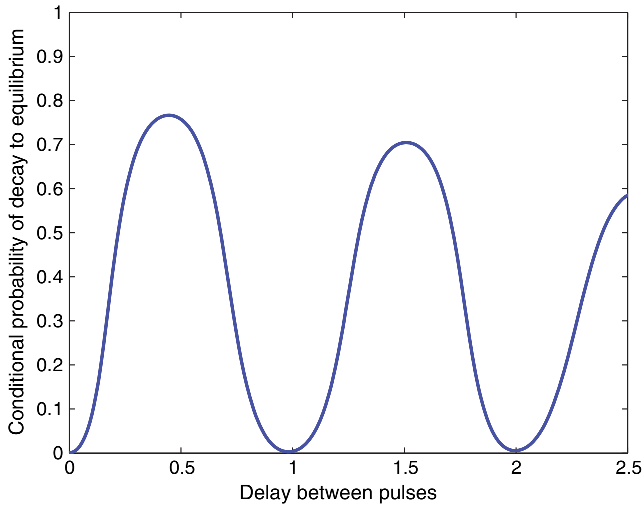

Fig. 13 Conditional probability of decay to equilibrium as a function of the delay between pulse and antipulse.

Figure 14 shows the conditional probability of decay to equilibrium as a function of the delay between the two pulse pairs. Again, we can see that an antipulse with a delay that is an odd multiple of $\tau_F/2$ can cause a decrease to the initial operating condition of a uniform pressure at 200 atm.

For a more detailed exploration of using the second pulse as a stabilizing agent, we fix the magnitude of the first pulse and consider the probability of decay to standard operating conditions for an antipulse that is controlled but for which the parameters (specifically, its delay and magnitude) retain some variability: this variability accounts for the fact that a practical control system requires a certain error margin.

Figure 15 shows, for a destabilizing pulse of 50% magnitude, the probability of decay as a function of the delay between the pulse and antipulse. Two cases have been considered: one in which the potential control system generates a strong antipulse, of magnitude in the 70–100% range, and one for a weaker antipulse of magnitude 50–100%

It can be seen that, for the strong antipulse, the probability of decay to the standard operating conditions is high when the time delay is close to an odd multiple of $\tau_F/2$, and it is particularly high for antipulses with a shorter time delay (the maximal probability of decay) near $0.5\tau_F$, which is almost one for a strong antipulse. It can also be seen that the reduction of the antipulse's strength reduces the possibility of decay considerably, by as much as 0.15 at the local maxima near $0.5\tau_F$, $1.5\tau_F$, and $2.5\tau_F$.

We also examine the probability of decay as a function of the fractional magnitude of the antipulse for three antipulses for which the delays from the destabilizing pulse are approximately $0.5\tau_F$, $1.5\tau_F$, and $2.5\tau_F$. This is plotted in Fig. 16.

Once again, it is seen that control is achieved most easily when the antipulse follows quickly after the destabilizing pulse: for the time $0.4\tau_F$–$0.6\tau_F$ delay range, we can see that any antipulse of magnitude over 70% is almost guaranteed to cause a decay to standard operating conditions. For a longer time delay, the antipulse's magnitude would have to be increased to over 80% in order to obtain a significant probability of decay.

For a destabilizing pulse of a smaller magnitude, it is to be expected that control is achieved more easily, since the instability takes longer to grow. This is confirmed by Figs. 17 and 18, which plot the probability of decay as a function of the time delay of the antipulse and its magnitude, for a destabilizing pulse of magnitude 30%.

In these figures, it can be seen that the overall probability of decay is larger than that for the 50% magnitude destabilizing pulse; decay is almost certain for an antipulse of magnitude over 80% and a time delay in the 0.4–$0.6\tau_F$ and 1.4–$1.6\tau_F$ ranges. In conclusion, the results of this section suggest that an intentionally introduced antipulse caused by injector blockages can be a highly effective control strategy. This is especially true if the antipulse follows quickly after the destabilizing event and is in the correct phase with respect to it (although it does not have to be precisely timed).

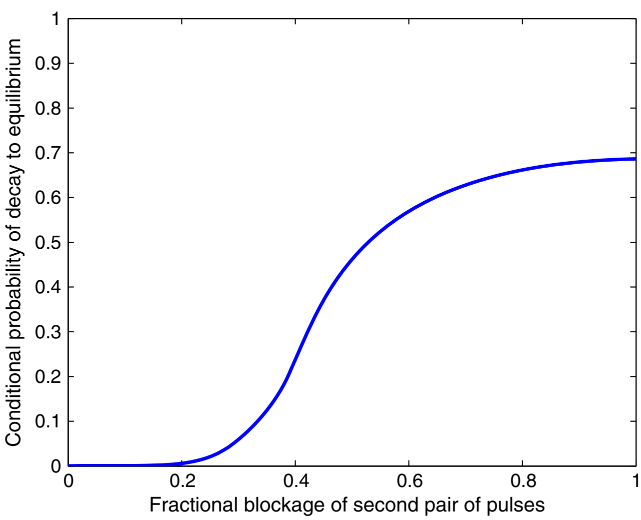

Fig. 14 Conditional probability of decay as a function of the fractional blockage for the second pair of pulses.

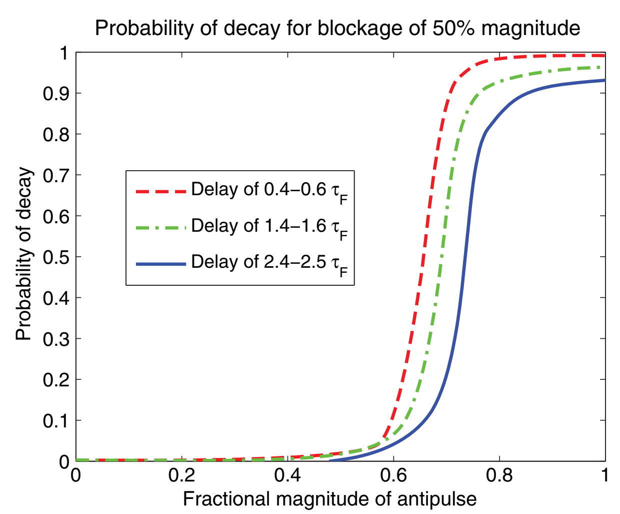

Fig. 16 Probability of decay to equilibrium as a function of the fractional magnitude of the antipulse, for a destabilizing pulse of magnitude 50%.

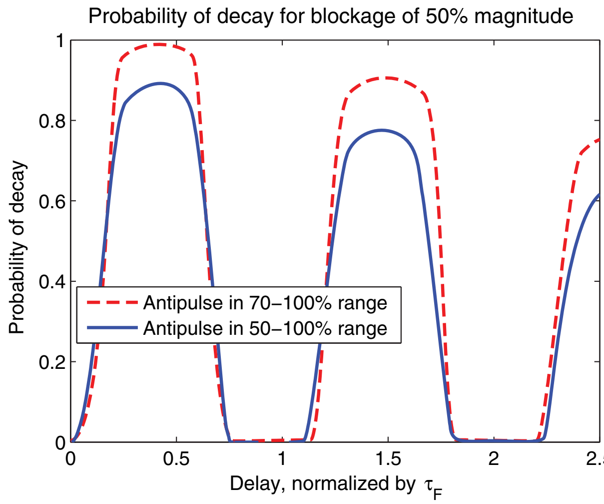

Fig. 15 Probability of decay to equilibrium as a function of the delay between pulse and anti-pulse, for a destabilizing pulse of magnitude 50%.

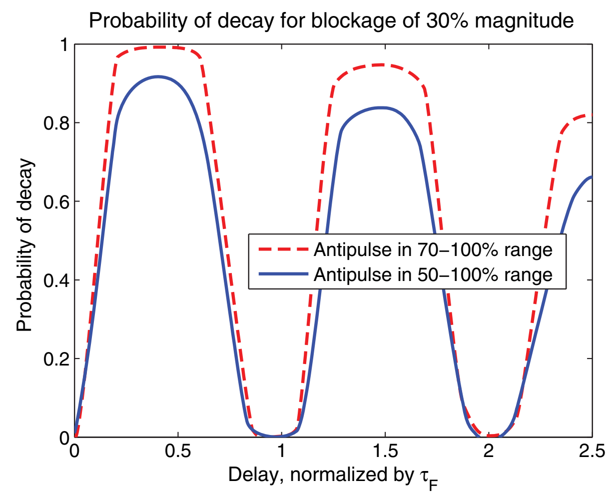

Fig. 17 Probability of decay to equilibrium as a function of the delay between pulse and antipulse, for a destabilizing pulse of magnitude 30%.

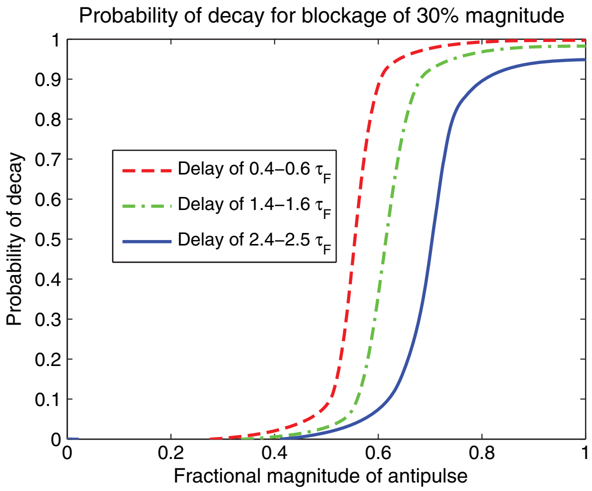

Fig. 18 Probability of decay to equilibrium as a function of the fractional magnitude of the antipulse, for a destabilizing pulse of magnitude 30%.

V. Conclusions

The method of stochastic simulation via polynomial chaos expansion for a LPRE combustion chamber, previously developed and described by Popov et al. [4], has been extended to include the effects of the injector feed system. A single blockage in the oxygen flow of an offcenter injector can cause the development of a standing wave first-tangential-mode limit cycle. Subsequent blockages, introduced either by accident or intentionally, can either modify the nature of the limit cycle to a traveling wave or bring about a decay of the limit cycle to the initial operating uniform pressure of 200 atm.

The capability of subsequent antipulses to bring about a decay of the instability decreases, as more time elapses since the triggering event. For a case in which considerable time has elapsed since triggering, and the instability has grown in magnitude, a single antipulse is not sufficient to cause a decay of the instability, but two antipulses closely following each other may have the desired effect.

It is found that the length of the injector channels have considerable influence on the stability characteristics of the system. When the channel's first longitudinal resonant mode is close in period to the first tangential mode of the combustion chamber, the injectors have a destabilizing effect, with higher probability for the development of a limit cycle, and a higher magnitude of the limit cycle than when the period of the injector's first longitudinal mode equals $3\tau_F/2$.

Overall, stochastic simulation via the PCE method provides a useful tool for the analysis of this highly complex system and for determining possible routes to control the development of instabilities in the LPRE combustion chamber.

Acknowledgments

This research was supported by the U.S. Air Force Office of Scientific Research under grant FA9550-12-1-0156 with Mitat Birkan as the Program Manager.

Reference

[1] Harrje, D., and Reardon, F. (eds.), "Liquid Propellant Rocket Combustion Instability," NASA TR-SP-194, U.S. Government Printing Office, 1972, Chap. 3.

[2] Oefelein, J. C., and Yang, V., "Comprehensive Review of Liquid-Propellant Combustion Instabilities in F-1 Engines," *Journal of Propulsion and Power*, Vol. 9, No. 5, 1993, pp. 657–677. doi:10.2514/3.23674

[3] Sirignano, W. A., and Popov, P. P., "Two-Dimensional Model for Liquid-Rocket Transverse Combustion Instability," *AIAA Journal*, Vol. 51, No. 12, 2013, pp. 2919–2934. doi:10.2514/1.J052512

[4] Popov, P. P., Sideris, A., and Sirignano, W. A., "Stochastic Modelling of Transverse Wave Instability in a Liquid Propellant Rocket Engine," *Journal of Fluid Mechanics*, Vol. 745, April 2014, pp. 62–91. doi:10.1017/jfm.2014.96

[5] Culick, F. E. C., *Unsteady Motions in Combustion Chambers for Propulsion Systems, AGARDograph AG-AVT-039*, NATO, Neuilly-sur-Seine, France, 2006.

[6] Summerfield, M., "A Theory of Unstable Combustion in Liquid Propellant Rocket Motors," *Journal of the American Rocket Society*, Vol. 21, No. 5, 1951, pp. 108–114. doi:10.2514/8.4374

[7] Crocco, L., and Cheng, S.-I., *Theory of Combustion Instability in Liquid Propellant Rocket Motors, AGARD Monograph 8*, Butterworths, London, 1956.

[8] Hutt, J. J., and Rocker, M., "High-Frequency Injector-Coupled Combustion Instability," *Liquid Rocket Engine Combustion Instability*, edited by Yang, V., and Anderson, W., Vol. 169, Progress in Astronautics and Aeronautics, AIAA, Washington, D.C., 1995, pp. 345–376.

[9] DeBenedictus, M., and Ordonneau, G., "High Frequency Injection Coupled Combustion Instabilities Study of Combustion Chamber/Feed System Coupling," *Joint Propulsion Conference*, AIAA Paper 2006-4721, 2006.

[10] Yang, V., Habiballah, M., Hulba, J., and Popp, M. (eds.), *Liquid Rocket Combustion Devices: Aspects of Modeling, Analysis, and Design*, Vol. 200, Progress in Astronautics and Aeronautics Series, AIAA, Reston, VA, 2005, Chaps. 1, 2, 4.

[11] Swithenbank, J., and Sotter, G., "Vortex Generation in Solid Propellant Rocket," *AIAA Journal*, Vol. 2, No. 7, 1964, pp. 1297–1302. doi:10.2514/3.2535

[12] Xiu, D., and Karniadakis, G., "The Wiener-Askey Polynomial Chaos for Stochastic Differential Equations," *SIAM Journal on Scientific Computing*, Vol. 24, No. 2, 2002, pp. 619–644. doi:10.1137/S1064827501387826

[13] Xiu, D., *Numerical Methods for Stochastic Computations: A Spectral Method Approach*, Princeton Univ. Press, Princeton, NJ, 2010, Chap. 6.

[14] Wiener, N., "The Homogeneous Chaos," *American Journal of Mathematics*, Vol. 60, No. 4, 1938, pp. 897–936. doi:10.2307/2371268

[15] Cameron, R., and Martin, W., "The Orthogonal Development of Nonlinear Functionals in Series of Fourier-Hermite Functionals," *Annals of Mathematics*, Vol. 48, No. 2, 1947, pp. 385–392. doi:10.2307/1969178

[16] Chehroudi, B., "Recent Experimental Efforts on High-Pressure Supercritical Injection for Liquid Rockets and Their Implications," *International Journal of Aerospace Engineering*, Vol. 2012, 2012, Paper 121802. doi:10.1155/2012/121802

[17] Davis, D. W., and Chehroudi, B., "Measurements in an Acoustically-Driven Coaxial Jet Under Supercritical Conditions," *Journal of Propulsion and Power*, Vol. 23, No. 2, 2007, pp. 364–374. doi:10.2514/1.19340

[18] Davis, D. W., and Chehroudi, B., "Shear-Coaxial Jets from a Rocket-Like Injector in a Transverse Acoustic Field at High Pressures," *44th AIAA Aerospace Sciences Meeting*, AIAA Paper 2006-0758, 2006, pp. 9173–9190.

[19] Leyva, I. A., Chehroudi, B., and Talley, D., "Dark Core Analysis of Coaxial Injectors at Sub-, Near-, and Supercritical Pressures in a Transverse Acoustic Field," *43rd AIAA/ASME/SAE/ASEE Joint Propulsion Conference and Exhibit*, AIAA Paper 2007-5456, 2007, pp. 4342–4359.

[20] Tucker, P. K., Menon, S., Merkle, C. L., Oefelein, J. C., and Yang, V., "Validation of High-Fidelity CFD Simulations for Rocket Injector Design," *44th AIAA/ASME/SAE/ASEE Joint Propulsion Conference and Exhibit*, AIAA Paper 2008-5226, 2008.

[21] Westbrook, C. K., and Dryer, F. L., "Simplified Reaction Mechanisms for the Oxidation of Hydrocarbon Fuels in Flames," *Combustion Science and Technology*, Vol. 27, Nos. 1–2, 1981, pp. 31–43. doi:10.1080/00102208108946970

[22] Westbrook, C. K., and Dryer, F. L., "Chemical Kinetic Modeling of Hydrocarbon Combustion," *Progress in Energy and Combustion Science*, Vol. 10, No. 1, 1984, pp. 1–57. doi:10.1016/0360-1285(84)90118-7

[23] Pope, S. B., *Turbulent Flows*, Cambridge Univ. Press, New York, 2000, p. 162.

[24] Petras, K., "Smolyak Cubature of Given Polynomial Degree with Few Nodes for Increasing Dimension," *Numerische Mathematik*, Vol. 93, No. 4, 2003, pp. 729–753. doi:10.1007/s002110200401

E. Kim
Associate Editor